Inorganic Chemistry

ARTICLE

pubs.acs.org/IC

Photoinduced Magnetism in Core/Shell Prussian Blue Analogue Heterostructures of $K_jNi_k[Cr(CN)_6]_l \cdot nH_2O$ with $Rb_aCo_b[Fe(CN)_6]_c \cdot mH_2O$

Matthieu F. Dumont,[†] Elisabeth S. Knowles,[‡] Amandine Guiet,[†] Daniel M. Pajerowski,[‡] Ariel Gomez,[§] Stefan W. Kycia,[§] Mark W. Meisel,*[,‡] and Daniel R. Talham*[,†]

[†]Department of Chemistry, University of Florida, Gainesville, Florida 32611-7200, United States

[‡]Department of Physics and the National High Magnetic Field Laboratory, University of Florida, Gainesville, Florida 32611-8440, United States

[§]Department of Physics, University of Guelph, Guelph, Ontario N1G 2W1, Canada

Supporting Information

ABSTRACT: Core/shell and core/shell/shell particles comprised of the Prussian blue analogues $K_jNi_k[Cr(CN)_6]_l \cdot nH_2O$ (**A**) and $Rb_aCo_b[Fe(CN)_6]_c \cdot mH_2O$ (**B**) have been prepared for the purpose of studying persistent photoinduced magnetization in the heterostructures. Synthetic procedures have been refined to allow controlled growth of relatively thick (50−100 nm) consecutive layers of the Prussian blue analogues while minimizing the mixing of materials at the interfaces. Through changes in the order in which the two components are added, particles with **AB**, **ABA**, **BA**, and **BAB** sequences have been prepared. The two Prussian blue analogues were chosen because **B** is photoswitchable, and **A** is ferromagnetic with a relatively high magnetic ordering temperature, ∼70 K, although it is not known to exhibit photoinduced changes in its magnetic properties. Magnetization measurements on the heterostructured particles performed prior to irradiation show behavior characteristic of the individual components. On the other hand, after irradiation with visible light, the heterostructures undergo persistent photoinduced changes in magnetization associated with both the **B** and **A** analogues. The results suggest that structural changes in the photoactive **B** component distort the normally photoinactive **A** component, leading to a change in its magnetization.

INTRODUCTION

Nanometer-scale effects of coordination polymers remain relatively unexplored compared to other classes of solids, such as semiconductors, metals, or metal oxides. For coordination polymers, the nanoscale affords an opportunity to take advantage of high and controllable surface-to-volume ratios, maximizing properties and processes that occur at the solid interface. Catalysis or separations come immediately to mind as areas that might benefit from such structures, but other important effects should also be enhanced such as charge transfer, electron transport, or spin interactions across solid−solid interfaces in optical, electronic, or magnetic devices or heterostructures. To take full advantage of interface effects, the ability to control coordination polymer synthesis on the nanoscale is required.

Although there are a few other examples,[1−3] the most extensively explored coordination polymer nanostructures are derived from Prussian blue and related Prussian blue analogues (PBAs), $A_jM^{II}_k[M'^{III}(CN)_6]_l \cdot nH_2O$. Techniques developed to synthesize coordination polymer particles mostly rely on organic coatings to control growth and stabilize the particles.[4] Notable examples include the use of the anionic surfactant sodium bis(2-ethylhexyl)sulfosuccinate by Mann et al.[5,6] to stabilize Prussian blue, while polymers such as poly(vinylpyrrolidone),[7] poly(ethylene glycol) mono-4-nonylphenyl ether[8] or the alkyl-based ligand didodecyldimethylammonium bromide[9] have been employed to stabilize different PBAs.

Recent interest in PBAs and related cyanide-bridged coordination networks is in the field of molecular magnetism. Examples of PBAs that are magnetic even at room temperature or above are known, but it is the light-induced effects that potentially set them apart from standard magnets.[10−16] The cobalt/iron analogue, $A_aCo_b[Fe(CN)_6]_c \cdot mH_2O$, where A is a monovalent cation, undergoes charge-transfer-induced spin transition (CTIST) from a diamagnetic to a paramagnetic state, which then magnetically orders below $T_c \sim 20$ K.[11−13,17,18] Similar effects have been observed for $Rb_jMn_k[Fe(CN)_6]_l \cdot nH_2O$.[19−21]

We recently reported the assembly of successive layers of two PBAs into nanometer-scale heterostructures that exhibited a photoresponse not seen in either constituent. Specifically, **ABA** films of the photomagnetic $Rb_{0.7}Co_{4.0}[Fe(CN)_6]_3 \cdot nH_2O$ (RbCoFe; $T_C \approx 18$ K), sandwiched between two layers of the ferromagnetic $K_{0.8}Ni_{4.0}[Cr(CN)_6]_{2.9} \cdot nH_2O$ (KNiCr; $T_C \approx 70$ K), which is not photoactive, showed large photoinduced changes in magnetization up to the ordering temperature of the KNiCr analogue.[22] The magnetic response of $A_jNi_k[Cr(CN)_6]_l \cdot nH_2O$ is known to be pressure-dependent,[23] and the results for the **ABA** films were attributed to structural changes in the photoactive RbCoFe component, causing strains within the adjacent KNiCr layers and thereby altering the magnetism. It is

Received: November 2, 2010
Published: April 20, 2011

important to emphasize that the unique photomagnetic response arises from the ability to form heterostructures of the two components because physical mixtures of the two components and mixed-metal solid solutions of the two phases do not show the same behavior.[24]

The unique behavior of the heterostructured film led us to investigate whether similar effects could be seen in other nanometer-scale heterostructures, such as core/shell particles. Synthetic routes to core/shell particles of Prussian blue analogues have already been described. In 2006, Brinzei et al.[25] reported a way to stabilize cyanometallate particles by electrostatics, without the use of surfactants. This method allows the surface of the particle to remain reactive, permitting the subsequent epitaxial growth of successive layers of different PBAs to generate elegant core/shell and core/shell/shell particles with dimensions of less than ~50 nm.[26]

The present report describes heterostructured particles of $Rb_aCo_b[Fe(CN)_6]_c \cdot mH_2O$ (**B**) with $K_jNi_k[Cr(CN)_6]_l \cdot nH_2O$ (**A**). In a previous study of **B** particles, we observed that magnetic order and persistent photoinduced magnetism is lost if particles are smaller than ~10 nm.[27] Also, the thin-film heterostructures that showed the cooperative effects between the two components had dimensions of approximately 200 nm/layer. Therefore, we targeted heterostructured particles of a somewhat larger scale than had previously been reported. Building on the methods of Catala et al.,[26] routes to building successive layers of around 50−100 nm of cyanometallate on preformed particles have been developed. The resulting particle heterostructures also exhibit the cooperative photomagnetic behavior reported previously in heterostructured thin films.

EXPERIMENTAL SECTION

Materials. $K_3Cr(CN)_6$ was synthesized by treating aqueous solutions of potassium cyanide with $CrCl_3 \cdot 6H_2O$ and used after recrystallization from methanol.[28] Deionized water used in synthetic procedures was obtained from Barnstead NANOpure. All of the other reagents were purchased from Sigma-Aldrich or Fisher-Acros and used without further purification. The filters used during the synthesis are Fast PES Bottle Top Filters with 0.2 or 0.45 μm pore size (Nalgene).

Core Particles. The synthesis was carried out at room temperature. An aqueous solution (100 mL) of $MCl_2 \cdot 6H_2O$ (M = Ni or Co, 0.40 mmol, 4 mM) and an equal volume of an aqueous solution containing $K_3M'(CN)_6$ (M′ = Fe or Cr, 0.45 mmol, 4.5 mM) were simultaneously added dropwise to 200 mL of nanopure water. In the preparation of RbCoFe particles, RbCl (0.8 mmol, 8 mM) was included in the $NiCl_2$ solution. The solution was kept under vigorous stirring for 1 h after complete addition. The particles were subsequently filtered under vacuum using a 0.45 μm filter for the RbCoFe particles and a 0.2 μm filter for the KNiCr particles before being washed with ultrapure water and before being redispersed in 100 mL of water for use in the next step. To isolate the particles, instead of water, the particles were redispersed in acetone and dried under reduced pressure.

*KNiCr Particle (**A**).* $K_{2.68}Ni_4[Cr(CN)_6]_{3.92}$. Light-green powder (76% yield). IR (KBr): 2174 (s, ν_{CN}, $Ni^{II}-NC-Cr^{III}$), 2124 (b, ν_{CN}, terminal $NC-Cr^{III}$) cm^{-1}. EDS (Ni/Cr): 6.54:5.84. Anal. Calcd for $C_{5.35}H_{1.28}N_{5.35}O_{0.64}K_{0.67}Ni_{1.00}Cr_{0.89}$: C, 22.91; H, 0.45; N, 26.73. Found: C, 23.54 ; H, 0.63; N, 27.95.

*RbCoFe Particle (**B**).* $Rb_{1.68}Co_4[Fe(CN)_6]_{3.00}$. Purple powder (93% yield). IR (KBr): 2159 (w, ν_{CN}, $Co^{II}-NC-Fe^{III}$(HS)), 2111 (w, ν_{CN}, $Co^{II}-NC-Fe^{III}$ (low-spin, LS)), 2093 (w, ν_{CN}, $Co^{II}-NC-Fe^{II}$) cm^{-1}. EDS: 13.7:49.2:36.9 (Rb/Co/Fe). Anal. Calcd for $C_{4.51}H_{3.02}N_{4.51}O_{1.52}Rb_{0.28}Co_{1.00}Fe_{0.75}$: C, 20.14; H, 1.11; N, 23.50. Found: C, 19.85; H, 0.93; N, 23.17.

Core/Shell Particles. The previously prepared core particle solution was diluted with water to 400 mL. An aqueous solution (200 mL) of $MCl_2 \cdot 6H_2O$ (M = Ni or Co, 0.76 mmol, 3.8 mM) and RbCl (1.5 mmol, 5 mM), when applicable, and an aqueous solution (200 mL) of $K_3M'(CN)_6$ (M′ = Fe or Cr, 0.84 mmol, 4.2 mM) were added dropwise (10 mL/h, peristaltic pump) under stirring at room temperature. Once the addition was complete, the particles were filtered using a 0.45 μm filter and rinsed with ultrapure water before being redispersed in 400 mL of water for use in the next step. To isolate the particles, instead of water, the particles were redispersed in acetone and dried under reduced pressure.

*KNiCr/RbCoFe Particles (**AB**).* Purple powder (94% yield). IR (KBr): 2160 (w, ν_{CN}, $Co^{II}-NC-Fe^{III}$ (high-spin, HS)), 2120 (w, ν_{CN}, $Co^{II}-NC-Fe^{III}$ (LS)), 2096 (w, ν_{CN}, $Co^{II}-NC-Fe^{II}$) cm^{-1}. EDS: 4.0:3.5 (Ni/Cr), 1.2:4.0:3.1 (Rb/Co/Fe).

*RbCoFe/KNiCr Particles (**BA**).* Purple powder (98% yield). IR (KBr): 2172 (w, ν_{CN}, $Ni^{II}-NC-Cr^{III}$), 2159 (w, ν_{CN}, $Co^{II}-NC-Fe^{III}$ (HS)), 2111 (w, ν_{CN}, $Co^{II}-NC-Fe^{III}$ (LS)), 2093 (w, ν_{CN}, $Co^{II}-NC-Fe^{II}$) cm^{-1}. EDS: 4.0:3.2 (Ni/Cr), 1.0:4.0:3.4 (Rb/Co/Fe).

Core/Shell/Shell Particles. To 400 mL of the previously synthesized core/shell particles was added an aqueous solution (300 mL) of $MCl_2 \cdot 6H_2O$ (M = Ni or Co, 1.0 mmol, 3 mM) and RbCl (1.5 mmol, 5 mM), when applicable, and a solution (300 mL) of $K_3M'(CN)_6$ (M′ = Fe or Cr, 1.2 mmol, 4 mM). The rate of addition was kept very low (10 mL/h, peristaltic pump) under stirring at room temperature. The particles were subsequently isolated by filtration using a 0.45 μm filter and washed with nanopure water. The particles were redispersed and washed with acetone and dried under reduced pressure.

*KNiCr/RbCoFe/KNiCr Particles (**ABA**).* Purple powder (97% yield). IR (KBr): 2173 (w, ν_{CN}, $Ni^{II}-NC-Cr^{III}$), 2160 (w, ν_{CN}, $Co^{II}-NC-Fe^{III}$ (HS)), 2120 (w, ν_{CN}, $Co^{II}-NC-Fe^{III}$ (LS)), 2096 (w, ν_{CN}, $Co^{II}-NC-Fe^{II}$) cm^{-1}. EDS: 4.0:2.8 (Ni/Cr), 1.2:4.0:3.2 (Rb/Co/Fe).

*RbCoFe/KNiCr/RbCoFe Particles (**BAB**).* Purple powder (97% yield). IR (KBr): 2167 (w, ν_{CN}, $Ni^{II}-NC-Cr^{III}$), 2158 (w, ν_{CN}, $Co^{II}-NC-Fe^{III}$ (HS)), 2113 (w, ν_{CN}, $Co^{II}-NC-Fe^{III}$ (LS)), 2093 (w, ν_{CN}, $Co^{II}-NC-Fe^{II}$) cm^{-1}. EDS: 4.0:3.3 (Ni/Cr), 1.1:4.0:3.1 (/Rb/Co/Fe).

Instrumentation. IR spectra were recorded on a Nicolet 6700 Thermo Scientific spectrophotometer. Typically, 64 scans are taken between 2200 and 1900 cm^{-1} with a precision of 0.482 cm^{-1}. Powder samples were mixed with KBr and pressed into a pellet using 3000 psi (20 MPa). A scan of pure KBr is taken as a background reference. Inductively coupled plasma mass spectrometry (ICP-MS) for elemental analysis on nickel, cobalt, chromium, and iron was performed by Complete Analysis Laboratories, Inc., Parsippany, NJ. Combustion analysis to determine carbon, hydrogen, and nitrogen (CHN) percentages was performed by the University of Florida Spectroscopic Services Laboratory. Transmission electron microscopy (TEM) was performed on a JEOL-2010F high-resolution transmission electron microscope at 200 kV. The TEM grids (carbon film on a holey carbon support film, 400 mesh, copper from Ted-Pella, Inc.) were prepared by dropping, onto the grid, 20 μL of a solution containing 5 mg of sample dispersed by sonication in 2 mL of EtOH for 30 min. Energy-dispersive X-ray spectroscopy (EDS/EDX) was performed with an Oxford Instruments EDS X-ray Microanalysis System coupled to the high-resolution TEM (HRTEM) microscope. A total of four scans were performed on different parts of the sample and then averaged to give relative atomic percentages for chromium and iron. Chemical formulas are based on the metal composition from EDS and ICP-MS, adding water and potassium as determined by the number of trivalent metal vacancies to ensure electroneutrality. Powder X-ray diffraction (XRD) diffractograms were

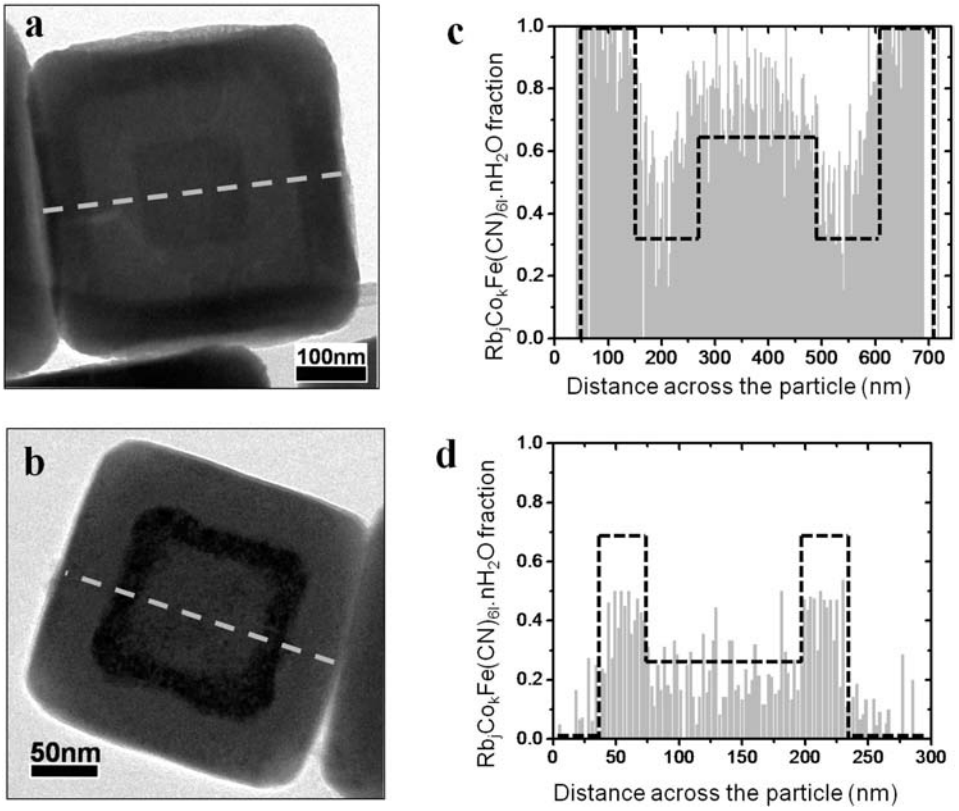

Figure 1. HRTEM images of the core/multishell particles and composition determined by EDS: (a) a RbCoFe/KNiCr/RbCoFe (**BAB**) particle; (b) a KNiCr/RbCoFe/KNiCr (**ABA**) particle; (c) the RbCoFe mole fraction across the particle in part a; (d) the RbCoFe mole fraction across the particle in part b. The dashed lines in parts a and b represent the path of the EDS line scan. In parts c and d, the predicted (dashed lines) and actual (solid columns) EDS line scan results are compared. The mole fractions were determined from line scans for the individual elements (see the Supporting Information).

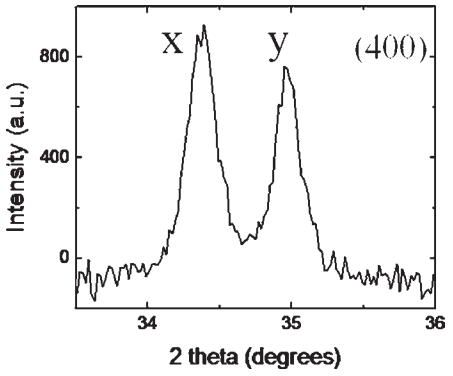

Figure 2. Room temperature XRD diffractogram of a sample of RbCoFe/KNiCr/RbCoFe (**BAB**) particles around the angle corresponding to the 400 plane. The peaks are assigned to (x) KNiCr, a = 10.42 Å, and (y) RbCoFe (HS), a = 10.26 Å.

recorded on a Philips APD 3720 powder diffractometer using a Cu Kα source. For the X-ray measurements, particles (50 mg) were mounted with double-sided tape on a glass slide. Magnetic measurements were performed using a commercial SQUID magnetometer (Quantum Design MPMS-XL7). Powder samples were applied to transparent tape, which was adhered around the circumference of a transparent drinking straw for mounting on a SQUID probe. A halogen light source (~1−2 mW), located at room temperature, was used to introduce light into the sample chamber of the SQUID through a bundle of 10 optical fibers (Ocean Optics model 200).

RESULTS

HRTEM images (Figure 1) show the well-defined shape of the particles with clear contrast between the core and different layers. In each TEM image, the RbCoFe layer appears darker than the KNiCr layer. The chemical assignments were confirmed from the EDS line scans across the particles, and the identity of each layer parallels the synthesis protocol. The line scans from the constituent elements (Supporting Information) were combined to map out the RbCoFe fraction across the particle shown in Figure 1. The composition profiles match well with those expected based on idealized core/shell/shell particle structures.

Powder XRD from a batch of RbCoFe/KNiCr/RbCoFe (**BAB**) particles can be indexed to two separate Prussian blue-like lattices using the space group $Fm\bar{3}m$ (No. 225). This point is most clearly shown using the (400) reflections (Figure 2), which provide nearly baseline-separated peaks. The peak positions correspond to the lattice constants for KNiCr, a = 10.42 Å, and HS RbCoFe, a = 10.26 Å. No peaks corresponding to a mixed phase with different lattice parameters could be detected, further confirming that the particles contain two different PBA compounds and that there is not extensive mixing of the transition-metal ions across the interface.[24]

The Fourier transform IR (FT-IR) spectra feature bands in the cyanide stretching region (1900−2200 cm^{-1}) expected for each compound (Supporting Information). Cobalt hexacyanoferrate gives peaks at 2163, 2120, and 2090 cm^{-1}, corresponding to the cyanide stretches of the Co^{II}−NC−Fe^{III} (HS), Co^{III}−NC−Fe^{II} (LS), and Co^{II}−NC−Fe^{II} (reduced) forms of the compound.

dx.doi.org/10.1021/ic1022054 |*Inorg. Chem.* 2011, 50, 4295–4300

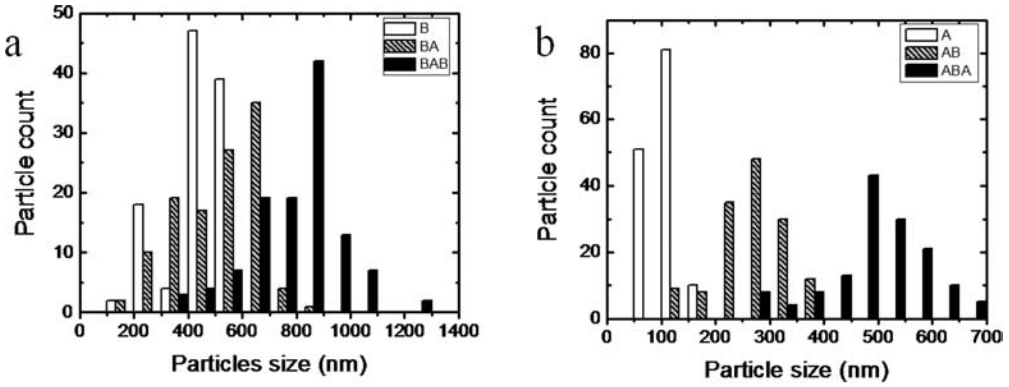

Figure 3. Size distribution of the particles after each step in the synthesis of **BAB** and **ABA** particles: (a) RbCoFe core (**B**), 443 ± 102 nm; RbCoFe/KNiCr (**BA**) core/shell, 502 ± 152 nm; RbCoFe/KNiCr/RbCoFe (**BAB**) core/shell/shell, 785 ± 163 nm; (b) KNiCr core (**A**), 110 ± 20 nm; KNiCr/RbCoFe (**AB**) core/shell, 266 ± 62 nm; KNiCr/RbCoFe/KNiCr (**ABA**) core/shell/shell, 493 ± 89 nm. For each sample, >150 particles were measured, taken from pictures of different areas on the TEM grid, using *ImageJ* software.[29]

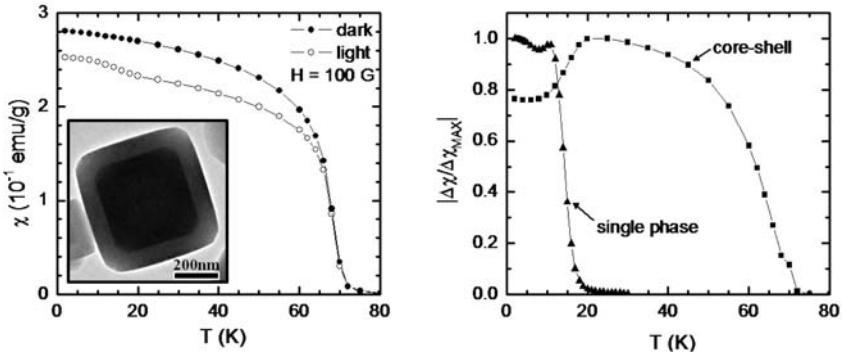

Figure 4. (a) Field-cooled magnetic susceptibility, χ, of **BA** as a function of the temperature before irradiation (●, "dark") and with the light off after 11 h of irradiation with visible white light (○, "light"). Lines are guides for the eyes. The inset is a HRTEM picture of a RbCoFe/KNiCr heterostructure. (b) Magnitude of the photoinduced change in χ, $\Delta\chi = \chi(\text{light}) - \chi(\text{dark})$, normalized to the maximum value: (■) data for the core/shell particles from the left panel; (▲) data for a single-phase Co/Fe PBA powder taken from ref 30. Lines are guides for the eyes.

The FT-IR spectrum of nickel hexacyanochromate displays a peak at 2160 cm^{-1}, corresponding to the bridged Ni^{II}—NC—Cr^{III} pairs. The multilayered heterostructures show combinations of these bands in the form of shoulders or broad peaks according to the relative amount of each component and its molar extinction coefficient. The relative molar extinction coefficients for each component were determined as described in the Supporting Information.

To better understand the growth of the particles, each step was followed by TEM and FT-IR to monitor how the size and chemical makeup evolves with consecutive shell additions (Supporting Information). Histograms of the particle sizes after each synthesis step show the particle growth (Figure 3). Using similar reactant concentrations for both phases, the histograms show that RbCoFe growth is slightly faster than KNiCr growth. The result is that the **ABA** particles described here are slightly smaller than the **BAB** particles.

The magnetic response of a batch of **BA** particles is shown in Figure 4. In the dark state, the temperature dependence of the susceptibility shows the expected onset of ordering above 70 K, characteristic of KNiCr, which dominates the response because of the larger ferromagnetic moment. Light-state data were obtained by first field-cooling the particles in the dark and then irradiating with visible white light, resulting in a significant decrease in magnetization. This photoinduced decrease is maintained up to 70 K, the characteristic ordering temperature of the KNiCr analogue. The light-state data also show the magnetic signature of the HS RbCoFe component, with an upturn in the susceptibility at its ordering temperature near 20 K. These features are also present in the other particle heterostructures, **AB**, **ABA**, and **BAB**, for which the magnitudes of the photoinduced changes correlate with the relative amounts of each component (Supporting Information). The response is the sum of the photoinduced decrease in magnetization associated with the KNiCr component below ∼70 K and the photoinduced increase associated with the RbCoFe component, which becomes important below ∼20 K. In the heterostructures with a larger KNiCr component, a photoinduced decrease is observed at all temperatures. If the particles contain enough RbCoFe, the photoinduced decrease in the susceptibility below ∼70 K turns to a photoinduced increase at ∼20 K and below (Figure S8 in the Supporting Information). The photoresponse parallels that observed for the heterostructured thin films of the same compounds described previously.[22] Relative to the photoactive single-phase RbCoFe, the important new behaviors observed for the heterostructured particles are the sign of the photoeffect and the fact that persistent photoinduced changes occur in the KNiCr component (Figure 4).

dx.doi.org/10.1021/ic1022054 |*Inorg. Chem.* 2011, 50, 4295–4300

DISCUSSION

Heterostructure Particle Synthesis. The synthesis of the core/shell Prussian blue analogue particles follows the basic process developed by Catala et al.[25,26] adapted to achieve larger particles, on the order of hundreds of nanometers. The need for larger particles derives from previous work on **B** that showed that particles of at least 10 nm in diameter were required to observe persistent photoinduced magnetism and ordering above 2 K.[26] Furthermore, the recently reported heterostructured films of **B** with $Rb_jNi_k[Cr(CN)_6]_l\cdot nH_2O$, for which new photoeffects were seen, had thicknesses of ~200 nm/layer.[21] Therefore, the present study targeted particles with 100−200 nm/layer.

The process begins with achieving a stabilized core, which becomes the site for the addition of the subsequent layers. An excess of the cyanometallate precursor in the core particle synthesis keeps the particles negatively charged, stabilizing the suspension without the use of surfactants. This method allows the surface of the particle to remain reactive, permitting the growth of successive layers of different PBAs at the surface.[26] Once the cores are washed and redispersed, it is imperative to control the diffusion of the precursors for the next layer so that they will react with the surfaces of the preformed core and avoid nucleation to generate new particles. Control is achieved by working with very dilute solutions and large volumes to minimize changes of the ionic strength during the addition steps. The rate of addition also proved to be extremely important. In order to avoid the formation of new nuclei, slow addition (10 mL/h) is used to avoid the buildup of precursors. The method described above yields particles that exhibit a sharp contrast between the two phases in the HRTEM pictures and well-defined XRD peaks. This approach accounts for a very clean interface with no detectable mixed phase. Scrambling of the ions to form mixed phases can dilute the magnetic properties, reducing T_c and masking the magnitude of the effects.[24]

The expectation is that the addition of shell layers will be favored if they can grow epitaxially on the existing particle surface. Defects are minimized and growth is favored if the characteristic intermetallic distances of the two PBAs are close enough to allow any lattice mismatch to be compensated for by the limited flexibility of the lattice. The Prussian blue analogues $Rb_jCo_k[Fe(CN)_6]_l\cdot nH_2O$ and $K_jNi_k[Cr(CN)_6]_l\cdot nH_2O$ have similar lattice constants, and the core/shell and core/shell/shell structures have been successful. On the other hand, attempts to grow such architectures with cobalt hexacyanochromate (a = 10.8 Å) and cobalt hexacyanoferrate (a = 9.92 Å for the LS phase and 10.25 Å for the HS phase), with a much larger difference in the unit-cell edge, have so far proven to be unsuccessful. For example, under the conditions described here to successfully prepare RbCoFe/KNiCr particles, attempts to add cobalt hexacyanochromate to the RbCoFe core resulted only in mixtures of single-component particles.

Magnetic Response. The photomagnetic response of the core/shell structure indicates that light-induced changes in the RbCoFe PBA core are transmitted to the KNiCr PBA shell, extending the ability to photoinduce changes in ordered state magnetization to temperatures well above T_c of $Rb_jCo_k[Fe(CN)_6]_l\cdot nH_2O$. The change in magnetization for the core/shell particles is the sum of the increase in magnetization of the RbCoFe analogue and the decrease in magnetization of the KNiCr component. Therefore, the magnitude of the photoinduced change in magnetization shifts near 20 K, the ordering temperature of RbCoFe (Figures 4 and S8 in the Supporting Information).

The behavior indicates that the initial light-induced changes occur in the RbCoFe lattice, which undergoes a charge transfer from $Fe^{II}-CN-Co^{III}$(LS) to $Fe^{III}-CN-Co^{II}$(LS), followed by a spin transition, giving the $Fe^{III}-CN-Co^{II}$(HS) state that is characteristic of this material.[10−12,16,17] This transition is conveyed to the shell, affecting the magnetism of the outer KNiCr layer. When the photoactive RbCoFe transitions from the LS state to the HS state, the metal-to-metal bond length increases by ~0.2 Å, enlarging the volume of the lattice. The expanding core will exert a mechanical stress on the adjacent KNiCr layer, the magnetism of which is known to be sensitive to pressure. Zentkova et al. showed that relatively small pressure changes induce large field-cooled magnetization changes in the low-temperature ordered state of $Ni_3[Cr(CN)_6]_2\cdot 12H_2O$, and this behavior was attributed to spin canting.[23] A field sweep of the heterostructures to achieve full saturation shows that the saturation magnetization actually increases in the light state (Supporting Information), confirming that spins have been created in the RbCoFe core. Therefore, the decrease of magnetization at low field does not result from a diminution of the number of moments.

The response of the heterostructured particles is remarkably similar to that of the analogous thin-film structures studied earlier. One difference is that the time constant for photoswitching is long relative to the related thin-film heterostructure (Supporting Information). This long time constant has been at least qualitatively reproduced for all of the core/shell samples, although additional studies are required to determine the origin of the slower kinetics.

CONCLUSIONS

New persistent photoinduced magnetization effects, first observed in **ABA** nanoscale thin films of **A** and **B**, have been extended to core/shell and core/shell/shell particle heterostructures of these same components, demonstrating that the new phenomena do not arise from the two-dimensional thin-film geometry previously studied. The heterostructured particles display a light-induced decrease in magnetization at temperatures as high as 70 K, the ordering temperature of the **A** component, which is not photomagnetic on its own. The observation of the new photoeffects in a second heterostructure geometry adds further support for the explanation that the structural change associated with the photoinduced CTIST in the **B** component induces strain in the adjacent **A** component, affecting its magnetization. The particle heterostructures are built by depositing successive layers of the alternating Prussian blue analogues on preformed particles, extending the procedure to a size regime not previously explored. This process, based on control of the addition rate of the metal precursors, provides clean interfaces even after deposition of relatively thick (50−100 nm) layers of the materials.

ASSOCIATED CONTENT

Supporting Information. Schematic of heterostructured particles along with a calculation of the expected EDS profile based on the particle architecture, as well as the EDS results for the individual metals in **ABA** and **BAB** heterostructures, the temporal evolution of the magnetic response for a **BA** heterostructure

during irradiation at 40 K and high-field magnetization at 2 K, a description of the synthesis protocol and procedures to determine the relative molar extinction coefficients for $Co^{III}-NC-Fe^{II}$ (LS), $Co^{II}-NC-Fe^{II}$ (reduced), and $Ni^{II}-NC-Cr^{III}$ pairs, FT-IR spectra for the RbCoFe core (**B**), RbCoFe/KNiCr (**BA**), RbCoFe/KNiCr/RbCoFe (**BAB**), the KNiCr core (**A**), KNiCr/RbCoFe (**AB**), and KNiCr/RbCoFe/KNiCr (**ABA**), magnetic susceptibility, χ, as a function of the temperature for **BAB**, **AB**, and **ABA** particles, and TEM images following each step in the preparation of core/shell/shell heterostructures. This material is available free of charge via the Internet at http://pubs.acs.org.

AUTHOR INFORMATION

Corresponding Author

*E-mail: talham@chem.ufl.edu (D.R.T.), meisel@phys.ufl.edu (M.W.M.).

ACKNOWLEDGMENT

This work was supported, in part, by NSERC, CFI, the U.S. National Science Foundation, through Grants DMR-1005581 (to D.R.T.) and DMR-0701400 (to M.W.M.) and the NHMFL via cooperative agreement NSF DMR-0654118 and the State of Florida. The authors thank Kerry Siebein at the University of Florida Major Analytical Instrument Center for HRTEM imaging and EDS analysis work.

REFERENCES

(1) Uemura, T.; Kitagawa, S. *Chem. Lett.* **2005**, *34*, 132–137.
(2) Dekrafft, K. E.; Xie, Z. G.; Cao, G. H.; Tran, S.; Ma, L. Q.; Zhou, O. Z.; Lin, W. B. *Angew. Chem., Int. Ed.* **2009**, *48*, 9901–9904.
(3) Galán-Mascáros, J. R.; Coronado, E.; Forment-Aliaga, A.; Monrabal-Capilla, M.; Pinilla-Cienfuegos, E.; Ceolin, M. *Inorg. Chem.* **2010**, *49*, 5706–5714.
(4) Larionova, J.; Guari, Y.; Sangregorio, C.; Guerin, C. *New J. Chem.* **2009**, *33*, 1177–1190.
(5) Vaucher, S.; Li, M.; Mann, S. *Angew. Chem., Int. Ed.* **2000**, *39*, 1793–1796.
(6) Vaucher, S.; Fielden, J.; Li, M.; Dujardin, E.; Mann, S. *Nano Lett.* **2001**, *2*, 225–229.
(7) Uemura, T.; Kitagawa, S. *J. Am. Chem. Soc.* **2003**, *125*, 7814–7815.
(8) Yamada, M.; Arai, M.; Kurihara, M.; Sakamoto, M.; Miyake, M. *J. Am. Chem. Soc.* **2004**, *126*, 9482–9483.
(9) Taguchi, M.; Yagi, I.; Nakagawa, M.; Iyoda, T.; Einaga, Y. *J. Am. Chem. Soc.* **2006**, *128*, 10978–10982.
(10) Ohkoshi, S.-i.; Tokoro, H.; Hozumi, T.; Zhang, Y.; Hashimoto, K.; Mathoniere, C.; Bord, I.; Rombaut, G.; Verelst, M.; Cartier dit Moulin, C.; Villain, F. o. *J. Am. Chem. Soc.* **2005**, *128*, 270–277.
(11) Sato, O.; Iyoda, T.; Fujishima, A.; Hashimoto, K. *Science* **1996**, *272*, 704–705.
(12) Sato, O.; Einaga, Y.; Fujishima, A.; Hashimoto, K. *Inorg. Chem.* **1999**, *38*, 4405–4412.
(13) Bleuzen, A.; Lomenech, C.; Escax, V.; Villain, F.; Varret, F.; Cartier dit Moulin, C.; Verdaguer, M. *J. Am. Chem. Soc.* **2000**, *122*, 6648–6652.
(14) Pejaković, D. A.; Manson, J. L.; Miller, J. S.; Epstein, A. J. *Phys. Rev. Lett.* **2000**, *85*, 1994.
(15) Gütlich, P.; Garcia, Y.; Woike, T. *Coord. Chem. Rev.* **2001**, *219−221*, 839–879.
(16) Pejaković, D. A.; Kitamura, C.; Miller, J. S.; Epstein, A. J. *Phys. Rev. Lett.* **2002**, *88*, 057202.
(17) Cartier dit Moulin, C.; Champion, G.; Cafun, J.-D.; Arrio, M.-A.; Bleuzen, A. *Angew. Chem., Int. Ed.* **2007**, *46*, 1287–1289.
(18) Ohkoshi, S.-i.; Hashimoto, K. *J. Photochem. Photobiol. C* **2001**, *2*, 71–88.
(19) Ohkoshi, S.-i.; Hamada, Y.; Matsuda, T.; Tsunobuchi, Y.; Tokoro, H. *Chem. Mater.* **2008**, *20*, 3048–3054.
(20) Lummen, T. T. A.; Gengler, R. Y. N.; Rudolf, P.; Lusitani, F.; Vertelman, E. J. M.; van Koningsbruggen, P. J.; Knupfer, M.; Molodtsova, O.; Pireaux, J. J.; van Loosdrecht, P. H. M. *J. Phys. Chem. C* **2008**, *112*, 14158–14167.
(21) Moritomo, Y.; Hanawa, M.; Ohishi, Y.; Kato, K.; Takata, M.; Kuriki, A.; Nishibori, E.; Sakata, M.; Ohkoshi, S.; Tokoro, H.; Hashimoto, K. *Phys. Rev. B* **2003**, *68*, 144106.
(22) Pajerowski, D. M.; Andrus, M. J.; Gardner, J. E.; Knowles, E. S.; Meisel, M. W.; Talham, D. R. *J. Am. Chem. Soc.* **2010**, *132*, 4058–4059.
(23) Zentková, M.; Arnold, Z.; Kamarád, J.; Kavečanský, V.; Lukáčová, M.; Mat'aš, S.; Mihalik, M.; Mitróová, Z.; Zentko, A. *J. Phys.: Condens. Matter* **2007**, *19*, 266217.
(24) Pajerowski, D. M.; Gardner, J. E.; Talham, D. R.; Meisel, M. W. *J. Am. Chem. Soc.* **2009**, *131*, 12927–12936.
(25) Brinzei, D.; Catala, L.; Louvain, N.; Rogez, G.; Stephan, O.; Gloter, A.; Mallah, T. *J. Mater. Chem.* **2006**, *16*, 2593–2599.
(26) Catala, L.; Brinzei, D.; Prado, Y.; Gloter, A.; Stéphan, O.; Rogez, G.; Mallah, T. *Angew. Chem., Int. Ed.* **2009**, *48*, 183–187.
(27) Pajerowski, D. M.; Frye, F. A.; Talham, D. R.; Meisel, M. W. *New J. Phys.* **2007**, *9*, 222.
(28) Bigelow, J. H. *Inorg. Synth.* **1946**, *2*, 203–205.
(29) *ImageJ* software, available at http://rsb.info.nih.gov/ij, developed by Wayne Rasband, National Institutes of Health, Bethesda, MD.
(30) Pajerowski, D. M., University of Florida, 2010.